ATLAS Internal Note
April 14, 2002

Electron Results for the ATLAS Electromagnetic Forward Calorimeter Module 0 Test Beam 1998

J.C. Armitage[a], L. Babukhadia[c], M. Dixit[a], T. Embry[c], V. Epshteyn[b], P. Estabrooks[a], P. Gravelle[a], J. Hamm[c], V. Khovansky[b], D. Koolbeck[c], P. Krieger[a], M. Losty[a], P. Loch[c*], J. Mayer[e], R. Mazini[d], G. Oakham[a], M. O'Neill[a], R. Orr[e], J. Rutherfoord[c], M. Ryabinin[b], A. Savine[c], C. J. Seely[c], P. Shatalov[b], L. Shaver[c], M. Shupe[c], G. Stairs[e], D. Tompkins[c], K. Vincent[e], and V. Zaitsev[b]

[a] *Carleton University, Ottawa, Ontario K1S 5B6, Canada*
[b] *ITEP Moscow, 117 259 Moscow, Russia*
[c] *University of Arizona, Tucson, Arizona 85721, USA*
[d] *University of Montreal, Montreal, Quebec H3C 3J7, Canada*
[e] *University of Toronto, Toronto, Ontario M5S 1A7, Canada*

[*] corresponding author

April 14, 2002

Abstract

The ATLAS Forward Calorimeter (FCal) is a unique calorimeter featuring cylindrical electrodes with thin tubular liquid argon gaps. The design is well adapted to meet the physics requirements for the forward region in the ATLAS experiment at the Large Hadron Collider (LHC) at CERN, Geneva, Switzerland. A pre-production module of the electromagnetic section (FCal1) was built at the University of Arizona in spring 1998 and subjected to particle beams, along with a hadronic FCal2 module built in Canada, at CERN's testbeam facility during the summer that year. In this note we present properties of the electron signal in the FCal1, including signal linearity well within the expectations of 1%, and a sufficient energy resolution with a constant term (high energy limit) of the order 4%. Comparisons to GEANT3.21 and GEANT4.2.0 based simulations are also shown, indicating that most of the relevant electromagnetic performance parameters can be described at the level of a few percent.

1 Introduction

The endcap and forward region (pseudorapidities $1.3 \leq |\eta| \leq 4.9$) in the ATLAS detector is instrumented with three different liquid argon calorimeters in the same cryostat. The Electromagnetic and Hadronic EndCap calorimeters (EMEC and HEC, respectively) cover the region $1.3 \leq |\eta| \leq 3.2$, while the three Forward Calorimeter modules (FCal1/2/3) close the acceptance gap to the beam pipe, up to about 4.9 in $|\eta|$, see Figure 1.

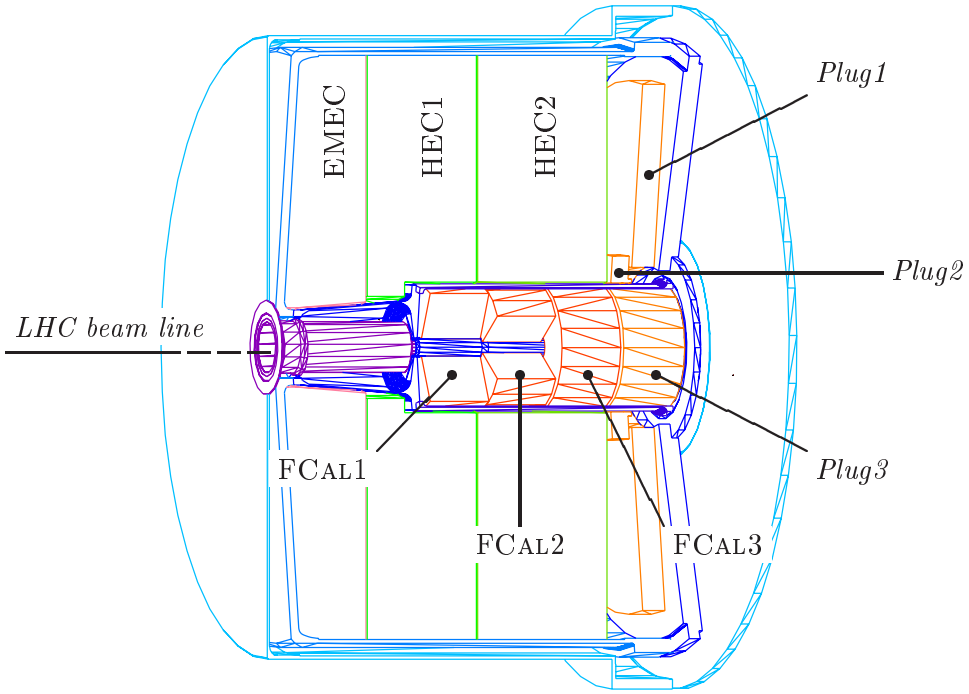

Figure 1: *The Forward Calorimeter in the ATLAS endcap cryostat. The three FCal modules FCal1, FCal2 and FCal3 are housed in the same cold vessel as the Electromagnetic EndCap and the two wheels of the Hadronic EndCap calorimeters. They are supported by a aluminum tube, is suspended from the front and rear cold walls of the cryostat. The brass cylinder located behind the FCal3 module (Plug3) is part of the shielding, together with a smaller brass ring around the rear part of the FCal support tube (Plug2), and a large brass disk mounted on the rear cold wall (Plug1).*

The electromagnetic Forward Calorimeter (FCal1) is a copper/liquid argon calorimeter, featuring thin tubular argon gaps. The hadronic modules FCal2 and FCal3 have the same electrode geometry, with tungsten as the absorber material (for more detailed descriptions of the calorimeters and their performances, see refs. [1] to [11]). Several prototypes for the electromagnetic module have been successfully tested in beams at Brookhaven National Laboratory and CERN (see refs. [3], [4] and [6]). Quarter segment, full depth pre-production prototypes for FCal1 and FCal2 ("Module 0's") have been designed and built in Arizona and Canada, respectively, in 1998, and submitted to an extensive test beam program with electrons, pions and muons at CERN the same year.

In this note we present results for electron signals in FCal1 Module 0. We start with

a description of the Module 0's in section 2, followed by an outline of the 1998 test beam setup from relevant beamline details to read-out electronics in section 3. Event selection and "beam cleaning" is discussed in section 4, followed by a description of the GEANT3.21 [12] and GEANT4.0.2 [13] setup used to simulate the electron response in section 5. Results for important electromagnetic performance parameters such as signal linearity and energy resolution are presented in section 6, together with comparisons to simulations. This section is followed by conclusions.

2 The Forward Calorimeter Module 0's

In this section we provide a description of the mechanics and readout organization of the FCal1 and FCal2 Modules 0's. Most of the features described here are similar for the final detector, with some minor changes in the readout structure at the inner and outer edge of the larger final modules.

2.1 Module mechanics

The FCal Module 0's are full depth quarter segments of the actual cylindrical modules, with 3/16 (1/4) of the final sensitive FCal1(2) volume instrumented. Both modules feature the tubular electrodes formed by thin wall copper tubes and copper (FCal1) or tungsten (FCal2) rods. The argon gap sizes are about 260 μm in FCal1[1], and 375 μm for FCal2, for electrode center-to-center distances of 7.5 and 8.179 mm, respectively. The argon gaps are maintained by nylon fiber of appropriate diameter wound around the FCal1 rods (Figure 2), and three PEEK spacers clipped onto the FCal2 rods. All spacers in the final modules are wound PEEK fibers, which are radiation hard (nylon is not) and have fewer mechanical problems than the clips.

The bulk absorber of FCal1 consists of 18 copper plates, each 2.5 cm thick, stacked to a total depth of 45 cm. This corresponds to about 29 radiation lengths (X_0) and 2.6 absorption lengths (λ). Each plate has 2351 holes drilled into it in a hexagonal pattern, to accommodate the electrodes, see Figure 2. The outer radius is about 45 cm. The inner beam hole has not been cut out of the plates, mainly to reduce the machining effort. The total weight of the module is approximately 0.5 t. Figure 3 shows the construction of the module in the cleanroom at Arizona.

The FCal2 absorber is built from small tungsten slugs, which fill the interstitial space between the tube electrodes. Two copper end plates hold the electrodes in position and contain the slugs inside the detector volume. The overall depth is 45 cm, which due to the much denser absorber corresponds to about 91 X_0 and 3.7 λ. The module weight is about 0.9 t. This module has 2550 individual electrodes in one quarter of the area of the final detector. A more detailed description of the hadronic Module 0 can be found in refs. [5] and [7].

[1] this is a slight variation from the original design gap width of 250 μm, introduced because of a somewhat better energy resolution for the larger gap [14].

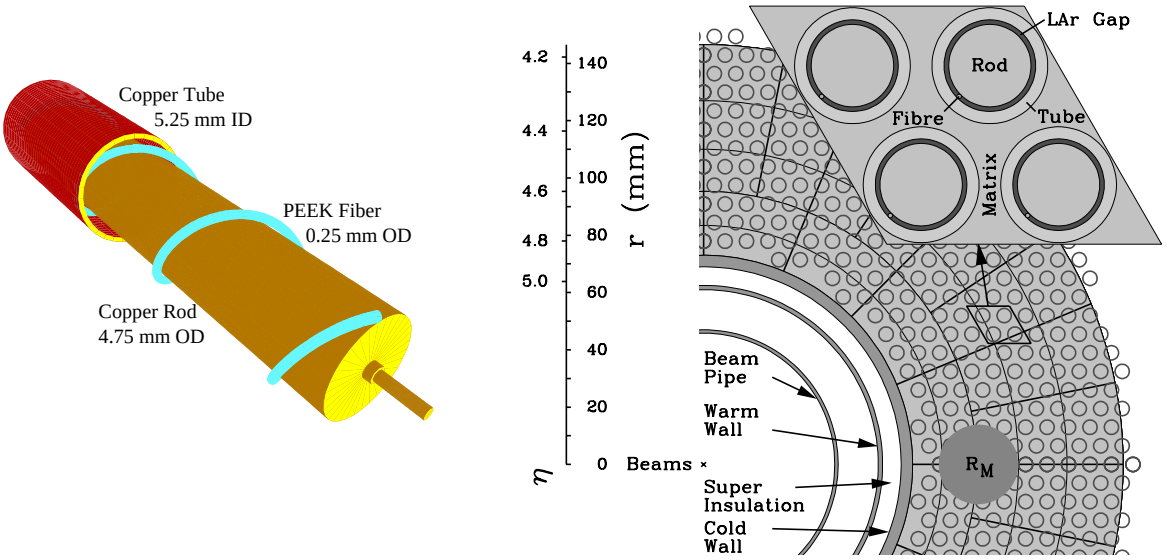

Figure 2: *One of the FCal1 tubular electrodes (left). The right figure shows the hexagonal electrode pattern in the absorber matrix. Also indicated is the Moliere Radius R_M for this calorimeter.*

2.2 Readout and cold electronics

Signals from individual electrodes are summed in two stages. First, small interconnect boards collect signals from groups of four(six) electrodes on the front(back) face of FCal1(2).

The signals from the electrode groups are then summed by fours again, except for the ones in the area closest to the beam pipe in ATLAS. Here the electrode groups are read out directly. This kind of summing introduces a pattern of small (four or six electrodes) and large (16 or 24 electrodes) tiles, each independently read out. The total number of tiles in the FCal1(FCal2) Module 0 is 192(128) (also see Figure 6 in the next paragraph).

The final stage summing is performed by auto-transformers, which take the four inputs into one output such that each input signal sees the same impedance. This avoids signal

Figure 3: *The FCal1 Module 0 absorber matrix during construction in the clean-room, with several electrodes already inserted.*

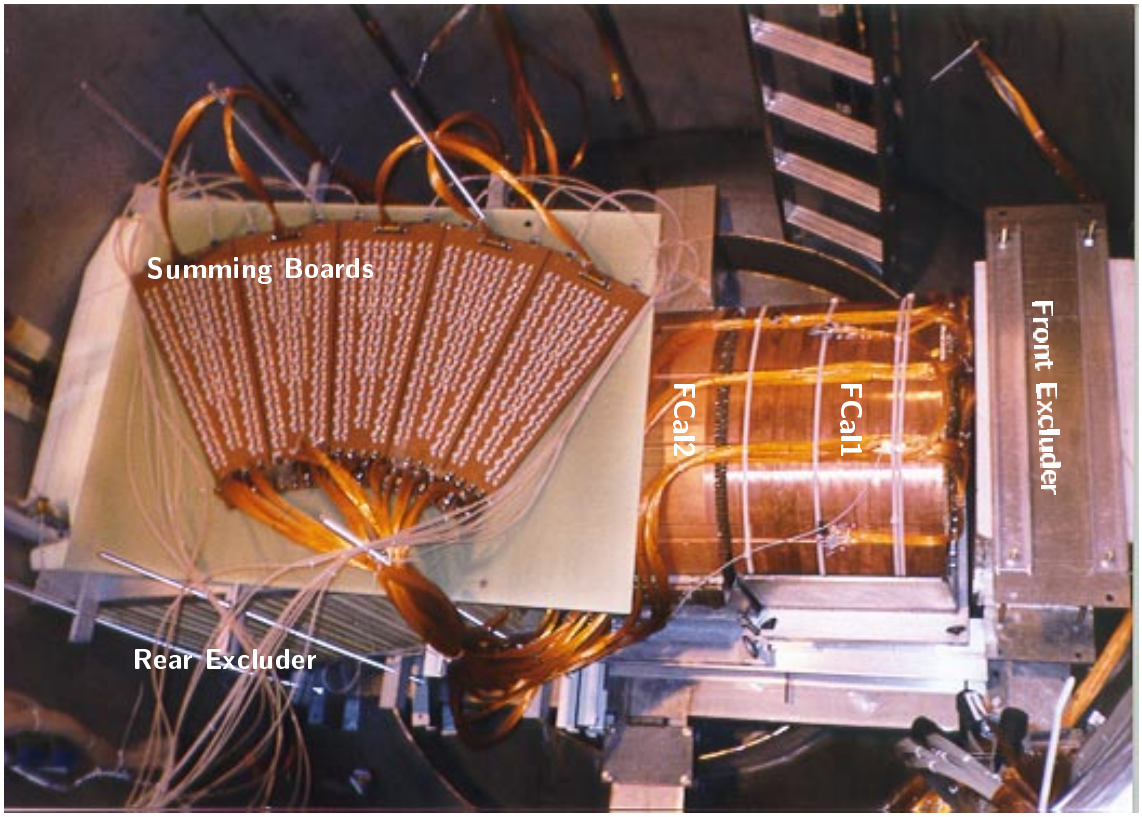

Figure 4: *FCal1 and FCal2 Module 0's in the H6C test beam cryostat at CERN. The photo also shows the summing boards and the front and back argon excluders.*

losses and actually allows signal summing with slightly less noise contribution than regular wire connections. The transformers are installed on summing boards, which each map 4×64 inputs from the electrode groups onto one 64-pin output. The cable run from the module interconnect boards to the summing boards is about 3.5 m. The cables are Kapton-wrapped coaxials with an impedance of 25 Ω.

The summing boards also handle the high voltage (HV) distribution (250 Volts for FCal1 and 375 Volts for FCal2) to the electrodes. There are four independent HV lines on each summing board, each assigned to one of the 64-pin input connectors. The HV is distributed to the individual electrode groups through a 1 MΩ protection resistor, and decoupled from the signal by a 12 nF capacitor.

The total of five summing boards are located in the liquid argon volume, close to the calorimeter modules. Three of the boards are used to form the 192 tile signals from FCal1 Module 0. The signals from FCal2 are formed on the remaining two boards. The summing boards for the Module 0's were mounted horizontally on a special frame on top of the rear argon excluder. The photograph in Figure 4 shows both Modules 0's in the H6C cryostat, with summing boards mounted, just before the commencement of the 1998 test beam run.

3 The Test Beam Setup

The summer 1998 test beam actually had two separate run periods, the first with the FCal2 Module 0 stand alone setup and the second with a combined FCal1/2 setup. In the following paragraphs we present some details of the beam line setup for the combined run, the triggers and the analog and digital readout electronics, which are relevant for the analysis presented in this note.

3.1 The FCal Module 0's in the test beam cryostat

The two FCal Module 0's have been mounted into the H6C cryostat at the end of the H6 beam line, see Figure 4. The electromagnetic FCal1 module is located in front of the hadronic FCal2 module. Upstream of FCal1, but still in the cryostat, is a piece of low density liquid argon excluder (Rohacell), to reduce the amount of inactive material in front of the calorimeter. Another piece of Rohacell is mounted directly behind the FCal2 module, thereby reducing the amount of material between the FCals and the first tail catcher scintillator.

Both modules are tilted by about 2.7°. The nominal impact position in the center of the module then corresponds to $\eta \approx 3.7$ in ATLAS, which is the direction of the largest longitudinal acceptance of the combined FCal1/2 system.

Several temperature probes are mounted on the modules to monitor liquid argon fill levels and temperature gradients in the liquid. The signal summing boards are mounted horizontally on top of the rear excluder, in contrast to the vertical mounting in ATLAS. This allows a lower liquid argon fill level in the test beam setup, without disturbing the functionality of the boards. High voltages are brought into the cryostat on single wire cables through a special feedthrough.

3.2 The beam line

The beam in H6 is a secondary particle beam provided by the SPS, which delivered electrons, pions and muons between 20 and 200 GeV/c momenta for the FCal test beam. The schematic depiction in Figure 5 shows the instrumentation of the FCal Module 0 beam line, starting directly after the last bending magnet, and including the various detectors used for online (hardware) triggering, the cryostat with calorimeter modules, the tailcatcher and beam stop, and the final muon scintillator counter.

The additional detectors in the beam line are used for triggering, various particle identifications, and position determinations. S1, S2, and S3 are scintillation counters providing the (fast) particle trigger by signal coincidence in all three counters. They are located far upstream (about 35 m) from the FCal Module 0's, close to the last vertical bending magnet.

Individual particle tracks can be reconstructed from signals from a set of multi-wire proportional chambers (MWPCs). These are set up along the flight path of the particles, starting close to the last bending magnet and going up to a few meters in front of the cryostat. The MWPCs employ two different readout technologies (delay time and wire hit pattern), with typically 64 wires at 1 mm spacing around the nominal beam position. Five chambers have both a horizontal and a vertical wire planes, and three chambers have either a vertical or horizontal plane only.

The veto system consists of a hole counter and a veto wall. The hole counter detects particles outside a 5 cm diameter circular area perpendicular to the nominal beam direction,

while the scintillators in the veto wall detect particles at larger distances from the beam.

The tailcatcher is a coarse iron/scintillator calorimeter located directly behind the cryostat containing the FCal detectors. Beyond the tailcatcher is a concrete beam stop followed by a single muon scintillator to record particles coming through the beam stop.

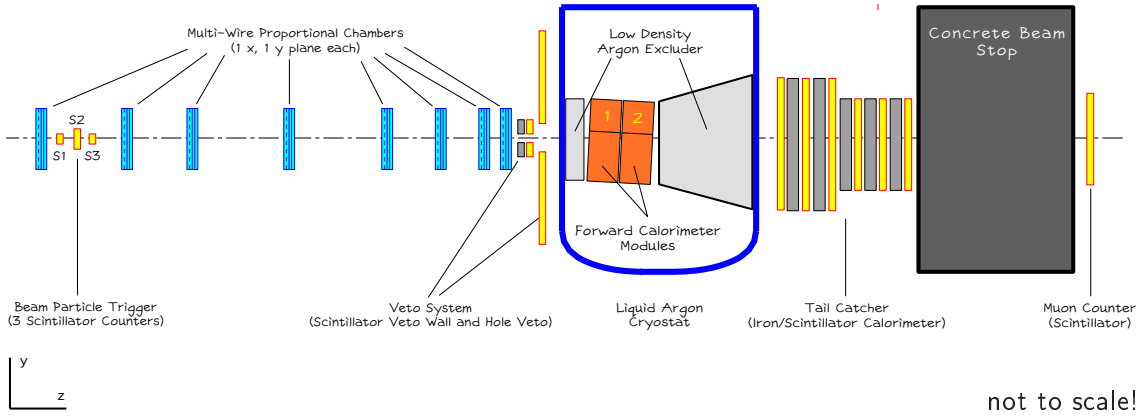

Figure 5: *Schematic view of the beam line instrumentation for the FCal test beam runs.*

3.3 Online triggers

The main event trigger is a low bias particle trigger. Each particle generating a signal corresponding to at least one minimum ionizing particle in each of the three scintillators S1, S2 and S3, is accepted as a valid event. Signals from the veto system, the tail catcher and the muon scintillator are latched into a trigger word, which is only used for fast event selection in the online monitoring and/or offline event reconstruction, i.e. there is no active veto in the hardware trigger at all. The data taking rate is only controlled by incoming particle flux (set by collimators in the beam) and the very short dead time of the acquisition system.

Monitor and random triggers are initiated during the particle burst as well, each at a rate of typically 5% of all triggers. The corresponding events help to monitor the whole system during actual data taking. Monitor triggers are events where all FCal channels are pulsed at the same time with a fixed pulse height. This allows measurement of the gain stability of the electronics. Random triggers are empty events used to measure the noise in the readout electronics. Like the monitor triggers, these events are initiated whenever there is a sufficient gap in the flow of incoming particle triggers, and the requested rate is not saturated.

Different logical combinations of trigger signals from S1 through S3, as well as signal sums from the the tail catcher and the muon counter, are used to flag possible electron, pion or muon event candidates, again latched into the trigger word. Some late and early pile up flags are also constructed from the hardware trigger information, to indicate events coming in too close together in time. None of these events are rejected online.

3.4 FCal analog readout electronics

The FCal signals are fed from the cold summing boards to the warm analog electronics through “pig-tail” cable harnesses (64 25 Ω Kapton cables, each about 4.5 m long). These connect the summing board outputs with the cold side of the feed-through flange. On the

warm side of this flange the signal is picked up by short (30 cm) 33 Ω stripline cables, which connect to the base-plane of the analog Front End Board (FEB) crate. This base-plane then transfers the signal to the input connector of the FEB. The base plane also provides the input pulse distribution network for electronic calibration and monitoring.

The FEB is a prototype design handling 128 inputs. Each of these inputs is connected to a pre-amplifier/shaper unit, which are packaged by fours (32 chips in total). The pre-amplifiers and shapers are very close to the standard ATLAS design [15].

The shaper has three gain stages on the output. For the test beam the high and medium gains are used. Standard read out for all tiles in FCal1 and FCal2 is high gain. 64 tiles in the center of FCal1 Module 0 and 32 tiles in the center of FCal2 Module 0 are read out with an additional medium gain, to accommodate higher energies: high gain saturation occurs at about 30(60) GeV of electron energy in a single channel in FCal1(2). The medium gain is about a factor of 10 less amplified and can therefore accommodate the full range of available beam energies ($20 - 200$ GeV). Figure 6 shows the bi-gain readout region for the two calorimeter modules.

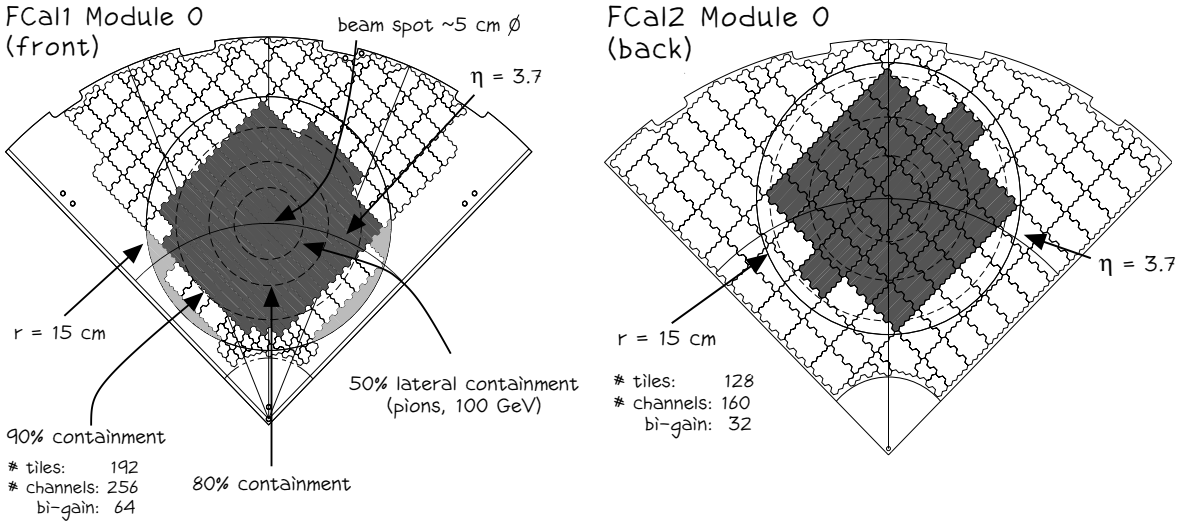

Figure 6: *Tiled readout on the FCal1 Module 0 front face (left) and the FCal2 Module 0 rear face (right). The dark gray areas indicate the size of the beam spot in the test beam. The light gray areas indicate channels (tiles) with bi-gain readout. The curved line shows the impact direction $\eta = 3.7$ in ATLAS.*

Each FEB handles 32 channels of bi-gain readout, meaning 160 output channels for the 128 inputs. The signals from the shapers are picked up by line drivers and sent to the data acquisition system in the counting house, through 35 m of individually shielded twisted pair warm cables (16 channels/cable).

3.5 Data Acquisition

The data acquisition (DAQ) for the 1998 test beam was very similar to the one used in the earlier FCal test beam efforts [6]. The signals on the warm cables were received by track & hold amplifiers (32 units/motherboard). Each of these track & holds produces a nearly

constant output signal when gated. The gate is produced by the fast trigger logic and timed such that the hold occurs at the peak of the signal. The duration of the hold gate is about 500 ns.

The hold signal is then digitized in 11-bit LeCroy FERAs (16 channels/unit), and read out through CAMAC. The FERAs are gated about 100 ns after the track & hold gate opens up. The integration time of the FERAs (gate width) is 100 ns. The CAMAC Look-At-Me (LAM) produced by the FERAs after digitization is done triggers the readout of the CAMAC crate through a 155 MHz Pentium PC. The trigger input is disabled for the duration of the readout.

The other detectors installed in the beam line are also read through CAMAC. The pulse heights in the beam counters and tail catcher are digitized by LeCroy 2249 ADCs (10 bits), while the hit pattern wire chambers are read through shift registers. The time delay wire chambers are read through a time-to-digital converter with 50 ps resolution. The hardware trigger word is formed through discriminators and two 16 bit output register. An event clock signal is provided by a 1 MHz clock and a 24 bit scaler. The whole readout is accommodated in two CAMAC crates.

The PC mentioned above reads the modules in the CAMAC crates and stores the event data in its internal memory. The particles in H6 arrive in bursts of about 2 seconds length, each 14 seconds apart. At the end of each burst the data is dumped to a disk mounted on an SGI Indigo R-4000 workstation. The reconstruction program running on this computer provides a fast first look at the signals while data is taken, in addition to a graphical event display.

About 35 million events were collected in total, at an average rate of about 400 Hz (about 800 events/spill). About 35 GBytes of disk space was filled in both run periods together.

4 Event Selection

One of the design features of the ATLAS Forward Calorimeter is the inhomogeneous front face. Depending on its impact position, the incoming particle may traverse a significant amount of relatively soft liquid argon before hitting the absorber, or hit the absorber first and start developing its shower earlier. Even though there is no significant tunneling, even at the relatively small impact angles with respect to the electrode orientation, a small signal variation has been observed and methods have been developed to correct for this effect using calorimeter information only (see paragraph 6.6 and refs. [2], [4] and [9]). High statistics with clean events and uniform illumination of a calorimeter region of at least the size of the lateral electrode dimensions with particles are needed to determine the average signal behavior, and to assure sufficient precision to develop and test impact point determination and signal correction methods. We therefore used beam optics which provided de-focussed beams close to the calorimeter location, and a system of MWPCs to provide track and vertex information on an event-by-event basis.

The H6 facility provides a rather clean electron beam for momenta between 10 and 80 GeV/c. Higher momentum beams typically have pion and muon contamination. Even though these particles are slightly separated in phase space, it was not always possible to sufficiently suppress them online by just setting collimators. Signals from the beam line and leakage detectors can be used, though, for further offline suppression. Several different methods were

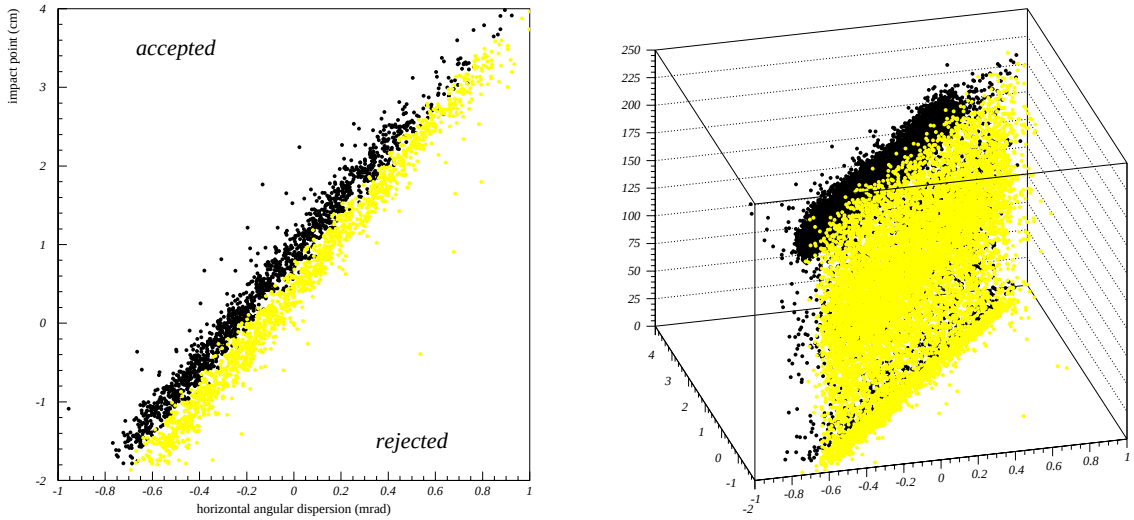

Figure 7: *The beam envelopes for electrons (black dots) and pions (gray dots) in the 200 GeV/c beam, as measured by the correlation between the horizontal deflection and impact point coordinate (left plot). The right plot shows the signal in FCal1 as function of the beam envelope – pions clearly generate the low energy tails in the signal spectrum.*

used to define a clean sample of electron events. These are described below.

4.1 Triggers

The recorded trigger pattern can be used offline as a first level event filter. An electron event is initially determined with hardware triggers by a coincidence of S1, S2, and S3 with no signal in the hole veto counter, and no tailcatcher energy recorded. This is very efficient for the lower energy runs up to 80 GeV/c particle momentum, but is less appropriate for the higher energy samples at 120 and 200 GeV/c, where the background from pions is significant. Suppression of this background using phase space information and reconstructed calorimeter quantities is discussed below. In-beam muons are more easily suppressed using the signal from the muon scintillator.

4.2 Particle tracking

Particle-by-particle track information is not only very useful to determine the impact point with relatively high precision (order 0.5 mm from the MWPCs), but also to measure the spatial separation[2] of the pion and electron beam at 200 GeV. This information can then be used to separate electrons and pions.

A particle track is defined by a linear fit using space points from hits in the MWPC's vertical and horizontal planes. Typically five space points per track are available. Events with more than one cluster in any of the chambers are rejected, as well as tracks measured with less than three space points or with low fit quality. The particle vertex in the vertical

[2]the phase space separation of electrons and pions in H6 is due to the additional energy losses of the electrons from bremsstrahlung, which reduces the actual electron energy at nominal 120(200) GeV to effective 119.0(193.7) GeV.

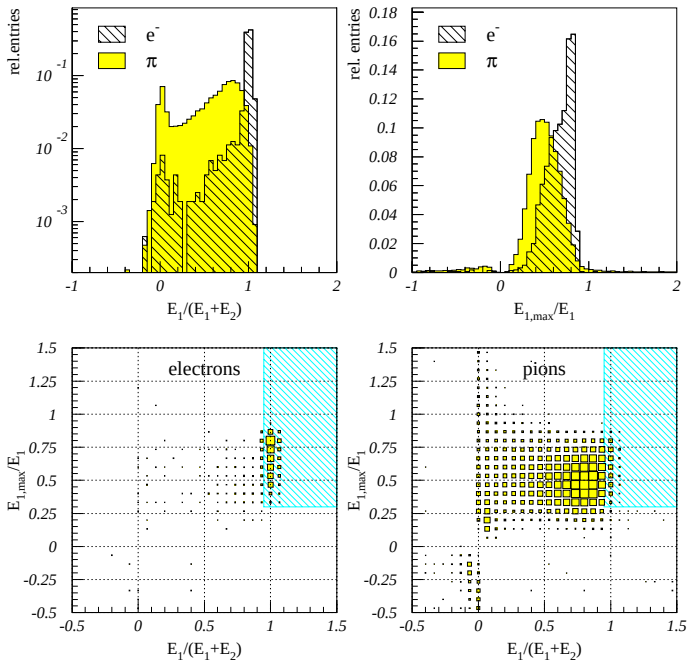

Figure 8: *Longitudinal containment and lateral shower compactness for 193.7 GeV/c electrons selected by the beam envelope cuts, see text (upper left and right plots). The distributions of the same variables for 200 GeV/c pions are shown in addition. The lower row shows the selection cuts in the space of these two variables (hatched areas), left for the pre-selected electrons, and right for pions.*

plane is determined by track extrapolation to the last bending magnet. The impact point is reconstructed in a vertical plane just in front of the calorimeter.

The "beam envelope" is defined by the horizontal and vertical deflection of the individual particle track from the nominal beam line, and the corresponding extrapolated impact point coordinate. This feature is used for 200 GeV/c beam. At this momentum the beam envelopes for electrons and pions are clearly separated, as can be seen in Figure 7.

Selections based on beam envelopes are unfortunately not very efficient for clean electron definition in the 120 GeV/c beam, because at this momentum the phase spaces for the different particles have a much larger overlap.

4.3 Electron definition using calorimetric variables

The selection strategies and cuts discussed so far make exclusive use of secondary detectors in the beam line, mainly the wire chambers. Additional improvement of the electron sample requires selections based on reconstructed calorimeter variables, without introducing biases in the electron event sample. The most obvious variables are those sensitive to the electromagnetic shower characteristics.

The FCal1 module is about 29 X_0 deep and is therefore expected to provide sufficient longitudinal containment for electromagnetic showers. In other words, the ratio of the energy E_1 in FCal1 to the total energy $E_1 + E_2$ in FCal1 and FCal2 can be expected to be close to unity. This reconstructed quantity is affected by the electronic noise, though, which can

be quite large[3] compared to the signals produced by the electrons at the (for this particular calorimeter) rather low test beam energies. This leads to large fluctuations in $E_1/(E_1+E_2)$. Still, this quantity is a good measure for longitudinal containment, as well as an efficient suppression of the pion background in the beam (Figure 8). The nonphysical region $E_1/(E_1+E_2) < 0$ is populated with events where noise dominates the signal sums. These events are rejected. $E_1/(E_1+E_2) > 1$ indicates events with negative noise in FCal2. These events are usually good electron candidates, and therefore kept in the sample.

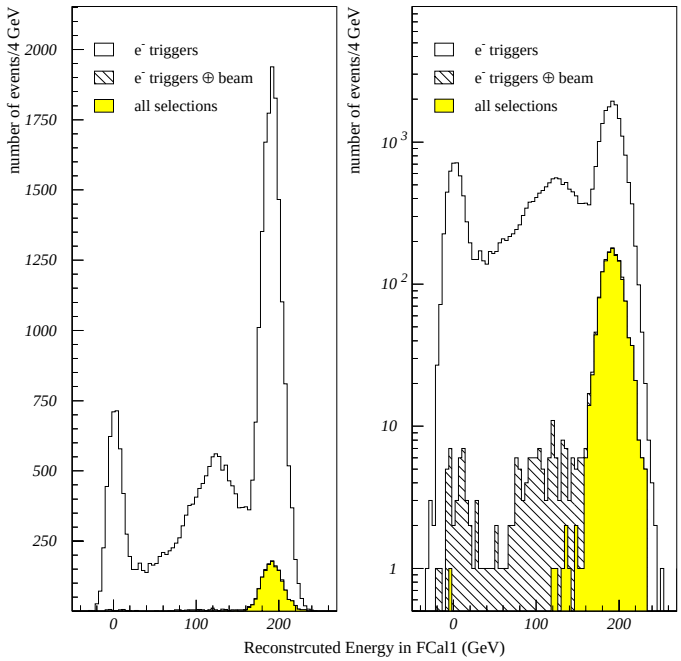

Figure 9: *Signal spectra for experimental signals from 193.7 GeV/c electrons after various selection cuts, shown on a linear (left) and semi-logarithmic scale (right).*

The other criteria used in the event selection derived from shower characteristics is the lateral electron shower compactness, compared to the typically wider hadronic showers. A sensitive measure of this feature is given by the ratio $E_{1,max}/E_1$, where $E_{1,max}$ is the energy in the FCal1 tile with the largest signal in a given event, and E_1 is the total energy in FCal1. A selection based on this ratio exploits the fact that the tile size in FCal1 is comparable to the Moliere Radius of the electromagnetic shower, so that most of the electron energy is typically deposited in one or two tiles only. Figure 8 shows the distribution for this variable and the final cuts in the $\{E_1/(E_1+E_2), E_{1,max}/E_1\}$ variable space.

The effect of the event selections on the signal spectra for 193.7 GeV/c electrons is shown in Figure 9. The selection by hardware trigger and the calorimetric variables cuts are applied for all energies, with a slight energy dependence of the acceptance threshold for $E_1/(E_1+E_2)$. The beam envelope cuts are only useful for the (nominal) 200 GeV/c beams.

[3]especially in FCal2, where the noise equivalent energy is boosted by a factor of about two with respect to FCal1, due to the different electron sampling fractions.

5 Electron Simulations

Although the major goals of the FCal Module 0 effort are the determination of calorimeter performance parameters, the collected data is naturally also useful for benchmark tests of shower simulation programs. This is especially important as we have to rely on Monte Carlo for predictions of the physics performance of the ATLAS detector. Verification of the simulations used in these studies in all possible detail, at least in the energy region accessible in test beams, can lead to increased confidence in the simulation predictions for different kinematic regimes.

The GEANT3.21 and the GEANT4.0.2 frameworks have been used to simulate the electron response in the FCal test beam setup. We describe some of the aspects of these two Monte Carlos used for comparisons with FCal1 Module 0 data in this section.

5.1 Geometry setup in the simulation

Specific care has been taken to completely describe the geometry of the FCal modules and the beam line elements. The geometries in GEANT3 and GEANT4 were set up in as similar a fashion as possible[4] in order to minimize systematic uncertainties in the comparison between the Monte Carlos and test beam data. We therefore do not differentiate between the two packages in the following discussion.

The test beam setup was described in sections 3.1 and 3.2. All detectors discussed there are implemented in the simulation, as are all other relevant inactive materials that may affect the signals from the various detectors. A picture of the region around the cryostat, taken from the GEANT4 setup, is given in Figure 10.

The description of the FCal modules is as close as possible to the real detectors. The electrode positions are directly read from the wiring database used in the module construction. This not only assures that the exact number of electrodes is implemented, but also allows establishing the correct relation between any given electrode and the corresponding readout channel in the simulation in a straight forward way.

The electrode geometry (length, inner/outer tube diameter, outer rod diameter etc.) is taken from averages of sample measurements on the real hardware, whenever available. The actual composition of all materials have been taken into account, whenever possible. Some simplifications had to made, though, to allow efficient simulation. For example, the FCal2 bulk absorber is not described at the level of individual tungsten slugs, but rather as a mixture of slugs (97% W, 2% Fe, 1% Ni), the liquid argon which fills the (small) spaces around the slugs, and the copper tubes forming the cathodes. The two copper endplates in this module are separate volumes in the simulation.

5.2 Particle generation

The inhomogeneous front face of the FCal introduces a slight dependence of the signal on the impact point, as mentioned earlier. The shape of the total signal spectrum therefore depends on the horizontal and vertical beam profile, i.e. how many electrons in a given sample hit argon first, and not the absorber material. To ensure an identical illumination in the simulations, we used reconstructed particle directions and vertices from the experiment

[4] both simulation packages use different methods to describe geometries.

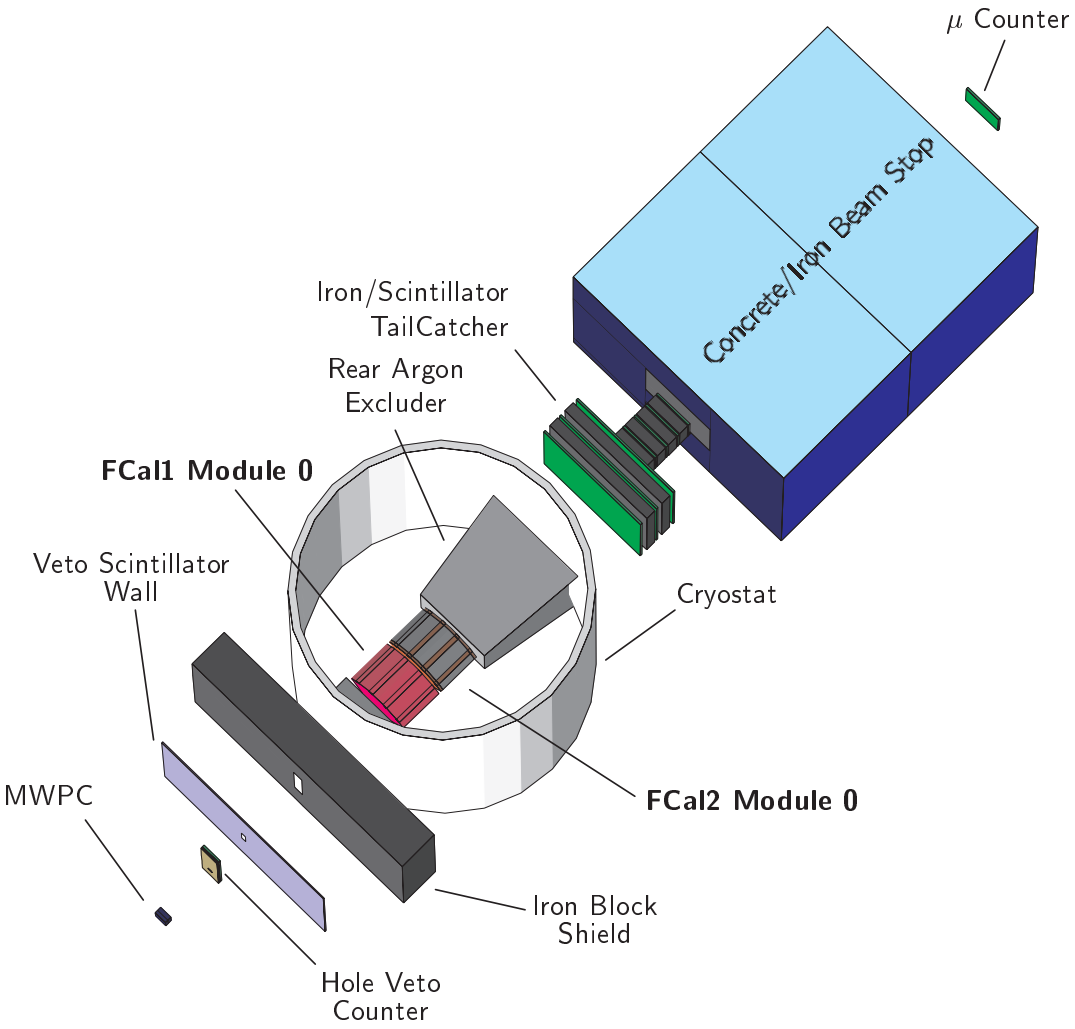

Figure 10: *A part of the FCal Module 0 test beam setup in GEANT4. Relevant beam line detectors, the cryostat including the two FCal Module 0's, the tailcatcher, the beam stop and the muon counter are shown. In this picture the particles enter the setup from the lower left corner.*

		GEANT3	GEANT4		
			0.5 mm	1.0 mm	2.0 mm
$E_{LAr}^{threshold}$	[keV]	10	4.4	6.18	8.67
$E_{Cu}^{threshold}$	[keV]	10	17.1	24.6	35.7
T_{CPU}	[s/GeV]	3.8	0.75	0.68	0.61
$1/c_{MC}$	[%]	1.44	1.42	1.41	1.36

Table 1: *Photon simulation parameters for GEANT3 and GEANT4 with various range cuts.* $E_{LAr}^{threshold}$ *and* $E_{Cu}^{threshold}$ *are the energy thresholds corresponding to the given ranges for photons in liquid argon and copper, respectively. The CPU time consumption* T_{CPU} *is measured on PIII 750 MHz machines.* $1/c_{MC}$ *is the sampling fraction.*

to generate particles in the simulation. This not only naturally generates the same beam profile, but also maintains the correlation between a given vertex and the track direction, as in the experiment.

The particle momentum in the test beam is known to about 0.5%. The initial momentum of the starting particle in the simulation has therefore been smeared by a Gaussian with the same width.

Secondaries generated by the initial electron along its path from the production vertex at the last bending magnet to the front cryostat wall are stored together with the response data from the various detectors. This allows tagging simulated electrons with energy losses due to bremsstrahlung. These events are usually rejected by tracking or high MWPC occupancy cuts in the experiment. The MWPC's are not explicitly simulated as active detectors, i.e. no attempt is made to simulate the wire responses.

5.3 Signal Reconstruction

The FCal signal in both the GEANT3 and GEANT4 simulations is the energy deposited in the liquid argon of the tube electrode. As in the experiment, the signals from the electrodes are summed into tiles, again using the wiring database to establish the relevant relationships.

The two simulation programs have different definitions of thresholds for particle tracking and secondary particle production. GEANT3.21 uses energy thresholds, while GEANT4 tracks particles to zero kinetic energy, but employs a minimum range requirement for production of secondaries in different materials. These cuts usually affect the simulated sampling fraction, as seen in table 1. For GEANT3 the lowest possible energy threshold of 10 keV is used in all materials; in case of GEANT4 range cuts of 0.5, 1.0 and 2.0 mm have been studied.

The experimental signal in a given tile is of course affected by the characteristics of the analog electronics, especially the noise, and the digitization. Some of these experimental inefficiencies have to be included in the reconstruction of the Monte Carlo signal, to allow a detailed comparison of all relevant energy variables. In particular the noise has to be taken into account for comparisons of the relative energy resolution. This is done by adding the signals from experimental randomly triggered "empty" events to the simulated signal E_{vis}^{tile}

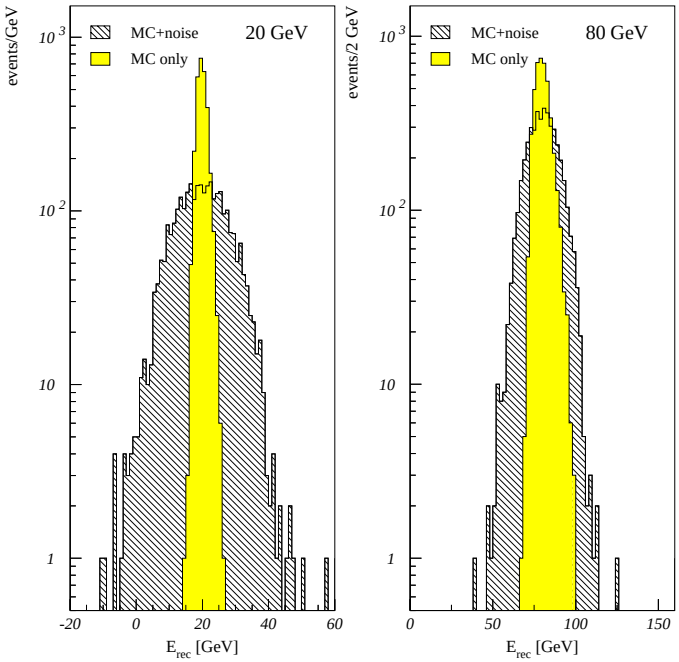

Figure 11: *Electron signals in FCal1, as simulated with GEANT3.21. Spectra are shown for the signals with and without noise added, for 20 (left) and 80 GeV/c momenta.*

tile by tile:

$$E_{rec}^{tile} = c_{MC} \cdot E_{vis}^{tile} + E_{noise}^{tile} \tag{1}$$

E_{rec}^{tile} is then the energy reconstructed in a given tile, c_{MC} the inverse sampling fraction in the simulation, and E_{noise}^{tile} the energy signal from the empty event. The later is given by

$$E_{noise}^{tile} = c_{exp} \cdot S_{noise}^{tile},$$

where S_{noise}^{tile} is the digitized signal from the random event (in counts), and c_{exp} is the experimental electron calibration constant. This parameter is calculated from the average response $\langle S \rangle$ [counts] of FCal1 to electrons of a given beam energy E_{beam}:

$$c_{exp} = E_{beam} / \langle S \rangle \quad [\text{GeV/count}]. \tag{2}$$

The effect of the noise on the signal spectrum for 20 and 80 GeV/c electrons in FCal1 is shown in Figure 11, where distributions of the visible and reconstructed energy, both summed over all tiles for each event, are compared.

6 Results

The most important performance requirements for an electromagnetic calorimeter are the direct proportionality of the signal to the incoming energy (signal linearity), and an adequate energy resolution. Each of these parameters has been studied in quite some detail for the FCal1 Module 0. The results are presented in this section, together with comparisons to GEANT3 and GEANT4[5] simulations.

[5]data produced with 0.5 mm range cut is shown, if not indicated otherwise.

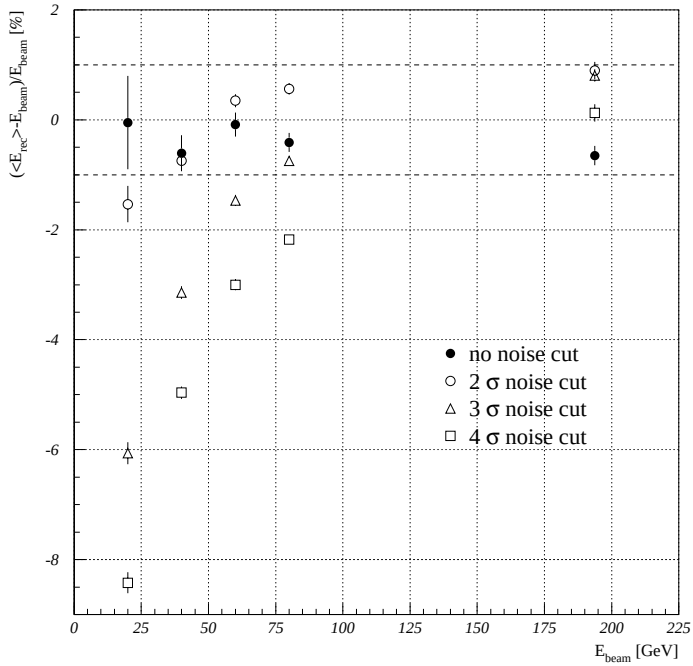

Figure 12: *Electron signal linearity, as measured in the test beam by the relative difference between reconstructed (E_{rec}) and beam energy E_{beam}, for different analysis methods, as function of the beam energy. The data is calibrated with the 60 GeV/c beam, without noise cut.*

6.1 Signal linearity

The electron signal E_{rec} in FCal1 Module 0 is reconstructed for all beam energies using the experimental calibration constant c_{exp} defined in eq.(2) in section 5.3. This constant has been calculated using the average signal of 60 GeV/c electrons. E_{rec} in a given event is

$$E_{rec} = c_{exp} \cdot \sum_{\text{tiles}} S^{tile} = \sum_{\text{tiles}} E_{rec}^{tile}, \tag{3}$$

where S^{tile} is the signal in tiles (channels) of FCal1 Module 0. The deviation from signal linearity is then defined as the relative difference between the average reconstructed energy and the beam energy $(\langle E_{rec} \rangle - E_{beam})\,/E_{beam}$. Figure 12 shows this difference for all available beam energies. The deviation from signal linearity for the unrestricted signal sum is well within $\pm 1\%$. Restricting the contributions to the sum in eq.(3) to tiles with signals satisfying the requirements

$$\underbrace{\left|E_{rec}^{tile}\right|}_{\left|c_{exp} \cdot S^{tile}\right|} > \nu \cdot ENE^{tile}, \tag{4}$$

where

$$ENE^{tile} = c_{exp} \cdot \sigma_{noise}^{tile}$$

is the energy equivalent of the electronic noise σ_{noise}^{tile} in a given tile and ν the chosen noise cut level, shows a stronger and more systematic deviation from linearity. This is expected,

as the noise cut tends to suppress true signal distributions in the sum[6], which leads to more severe relative signal losses at the lower beam energies. The somewhat surprising signal gain indicated in Figure 12, especially for $E_{beam} > 40$ GeV and a noise cut level of $\nu = 2$, shows that the total signal in the unrestricted sum is affected by small negative signals observed around the electromagnetic shower core. These have been identified as cross talk signals, which are of course suppressed by the noise cut. This observation is further discussed with the radial shower profiles in paragraph 6.4.

6.2 Response compared to simulations

The straightforward analysis of signal linearity presented in the preceding paragraph is sensitive to energy losses in upstream inactive material or beam line detectors[7]. These losses are to first order independent of the beam energy. The corresponding relative signal losses in the calorimeter are then a function of the beam energy, and therefore affect the deviation from linearity, as defined above. There is not a real, direct measurement of these losses in the experiment, certainly not event by event. The alternative approach outlined in the following is motivated by the ideas presented in [16].

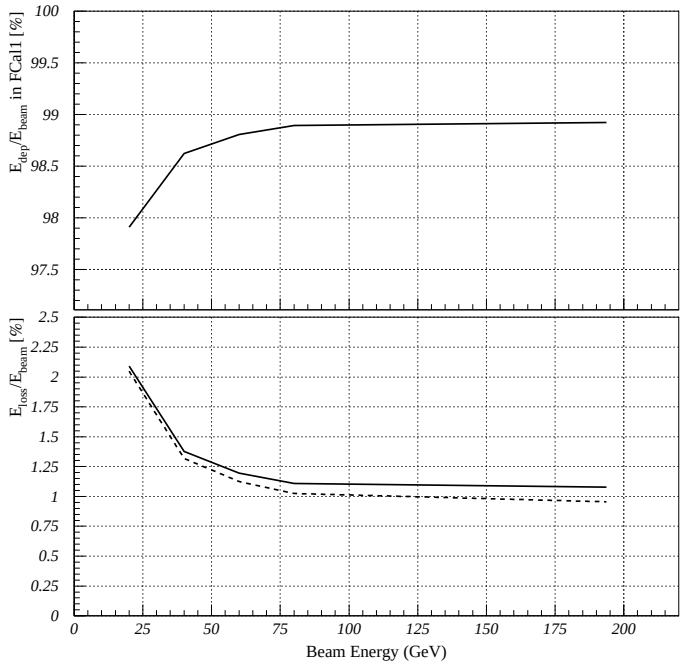

Figure 13: *Acceptance of FCal1 Module 0 for electrons, as measured with GEANT3 simulations by the ratio of energy deposited in the sensitive region of the detector E_{dep} over the beam energy E_{beam}, as function of E_{beam} (upper plot). The lower plot shows the energy losses with (solid line) and without (dashed line) longitudinal leakage (see text).*

A detailed simulation of the test beam experiment at least allows a determination of the average losses for a given beam energy. This is achieved by actually measuring the energy E_{dep}

[6] c_{exp} is always taken from the "no noise cut" analysis.

[7] the total amount of material upstream of the sensitive calorimeters, including cryostat walls, excluder and liquid argon, is about $1.5X_0$ in the 1998 FCal Module 0 setup.

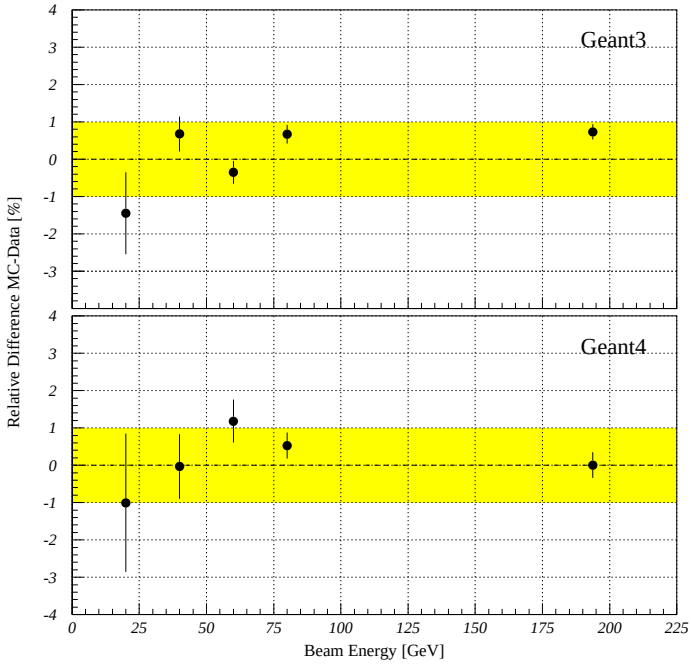

Figure 14: *Deviation from linearity, as defined in eq.(5), as function of the beam energy, for GEANT3 (top) and GEANT4 (bottom).*

deposited in the calorimeter module, which can then can be used to measure the acceptance, here defined as E_{dep}/E_{beam}. The dependence of this ratio on E_{beam} for the FCal1 Module 0 is shown in Figure 13. The lower plot in the same figure shows that most of the energy is indeed lost in front of the module – energy leakage to the back (and side) is insignificant. The relative effect is of the order of 1% at lowest beam energies.

Knowing the average deposited energy at each beam energy from simulations allows redefinition of the deviation from linearity as the relative difference between the average energy reconstructed in the simulation[8] $\langle E_{rec}^{mc} \rangle$ and the experiment $\langle E_{rec}^{exp} \rangle$:

$$\Delta L = \frac{\langle E_{rec}^{mc} \rangle - \langle E_{rec}^{exp} \rangle}{\langle E_{rec}^{exp} \rangle} \tag{5}$$

ΔL also tests the prediction power of the simulation for various energy reconstruction methods, as long as these are applied in exactly the same way to data and simulations. Figure 14 shows ΔL calculated using GEANT3 and GEANT4 simulations, with total signals reconstructed by summing all tile signals in one event, very similar to eq.(3). The tile energy signal E_{rec}^{tile} for the simulations includes the noise, see eq.(1) in paragraph 5.3.

Figure 15 shows the same ΔL for two energies reconstructed with different noise suppression cuts, i.e. using selective tile sums with a filter as given in eq.(4). Both simulations follow the experimental signal quite well in general, even though GEANT4 seems to be able to predict the average within $\pm 1\%$, while GEANT3 shows larger disagreements for higher noise cut levels ν ($2-4\%$, typically). This indicates a different relative weight of the noise in the reconstructed energies for the two different Monte Carlos.

[8] the simulations are intrinsically linear, as long as the amount of dead material in front of the detector is relatively small.

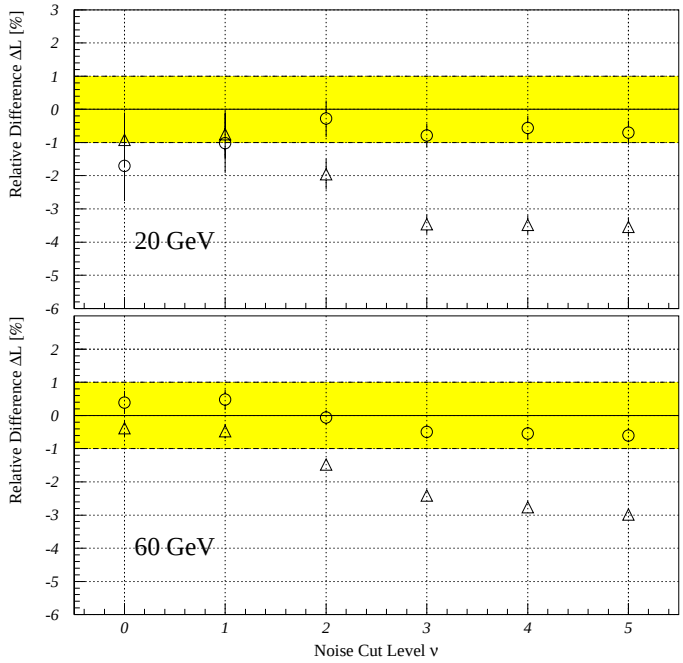

Figure 15: *Deviation from linearity for various noise cuts ν and two beam energies. The full circles are GEANT3 simulations compared to experimental data, while the open circles show the same comparison for GEANT4 simulations.*

It is also important to note that for this comparison the contribution of the negative signals from cross talk, as discussed in the previous paragraph, must be unfolded from the experimental response to allow a realistic comparison to the simulations. This has been done by using the maximum signal in the experimental radial shower profiles (see paragraph 6.4) as reference for ΔL.

6.3 Energy resolution

Figure 16 shows that not only the average responses for experiment and both simulations compare very well, but also the shape of the signal distributions look very similar. This is more quantitatively discussed below.

The relative energy resolution is given by $\sigma(E_{rec}) / \langle E_{rec} \rangle$, where both the width $\sigma(E_{rec})$ and the average $\langle E_{rec} \rangle$ are determined by an unrestricted Gaussian fit to the reconstructed energy (E_{rec}) distributions for various beam energies. The total energy has been calculated by summing all FCal1 channels for each event, which includes a rather large amount of noise – the significant part of the electron signal is typically found in one to four tiles only, depending on the impact point. Still, by adding the noise to the simulations, it is possible to describe the experimental resolution quite well with both GEANT3 and GEANT4, see Figure 17.

Selective tile energy sums using a noise cut (signal significance selection) as described in the previous paragraph, reduce the noise contribution to the relative energy resolution, as can be seen in Figure 18.

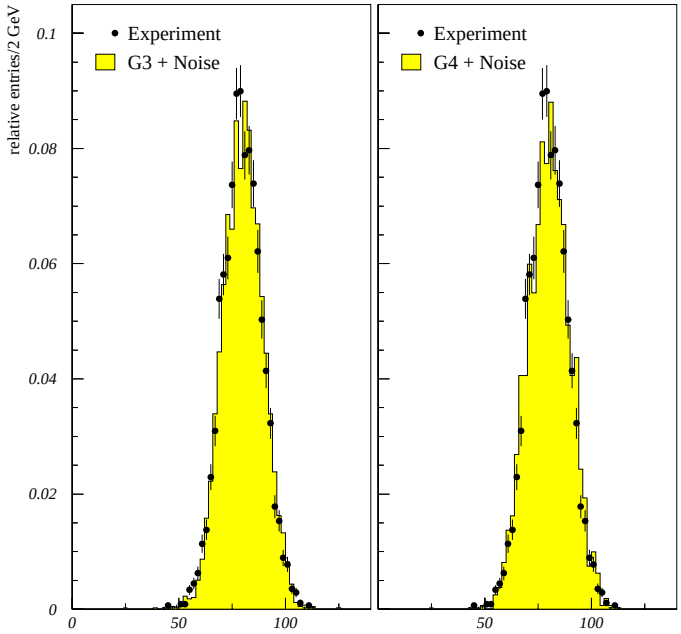

Figure 16: *The reconstructed energy spectrum for 80 GeV/c electrons in FCal1 Module 0. The experimental distribution is compared to GEANT3 (left plot) and GEANT4 (right).*

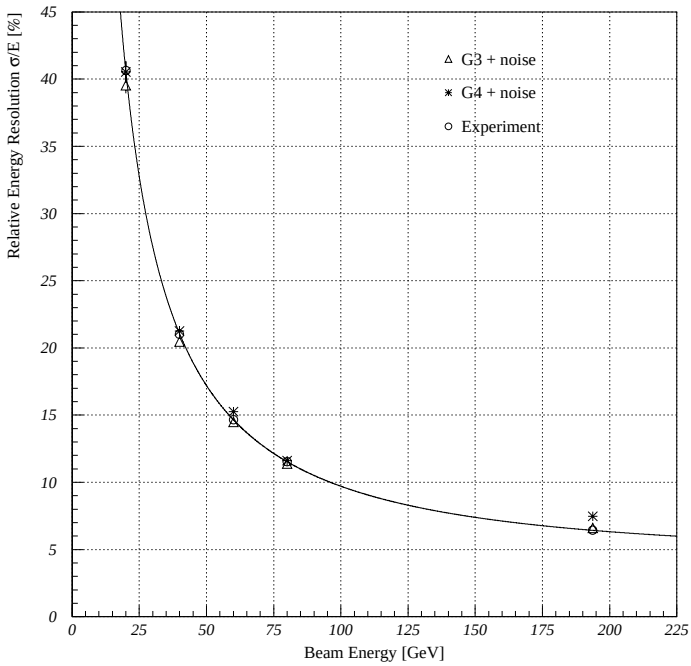

Figure 17: *The relative energy resolution for electrons in FCal1 Module 0, as function of the beam energy, for experimental data, GEANT3 and GEANT4.*

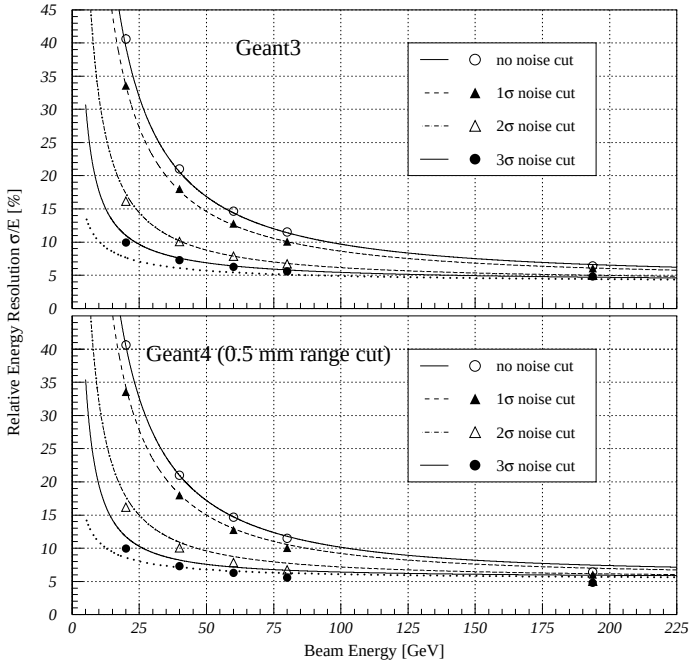

Figure 18: *The relative energy resolution for electrons in FCal1 Module 0, for several different noise cuts (data points – experiment, solid curves – simulations). The dotted curves show the best possible energy resolution, as predicted by GEANT3 or GEANT4, respectively, both without the noise or noise cut.*

The relative energy resolution can be described by

$$\frac{\sigma(E_{rec})}{E_{rec}} = \frac{a}{\sqrt{E_{beam}}} \oplus \frac{b}{E_{beam}} \oplus c, \tag{6}$$

where a is the stochastic term of the energy resolution, b is the noise term, and c is the constant term. The results from fits to the resolution curves for the various noise cuts ν are shown in Figure 19. Both simulations can describe the relative energy resolution quite well, with some remaining discrepancies for GEANT4.

6.4 Radial clustering

The noise suppression strategy based on cell selection, as used for the determination of the signal linearity and energy resolution in the previous paragraphs, has the disadvantage that potentially many tiles with small "true" signals can be lost. This can lead to rather poor linearity, especially at lower electron energies. An alternative approach is radial clustering, where the signal is collected in a cylinder around the particle impact point. The radius of the cylinder can be tuned such that the signal linearity is within the requirements, while the resolution is as close to the optimum as possible.

One of the problems with cylindrical clustering is that additional signal fluctuations can be introduced due to the readout granularity. Signals in tiles with geometrical centers outside the chosen cylinder are typically not included in the cluster signal, even if some fraction of the tile area is within the cylinder. Tiles with their geometrical centers inside the cylinder then

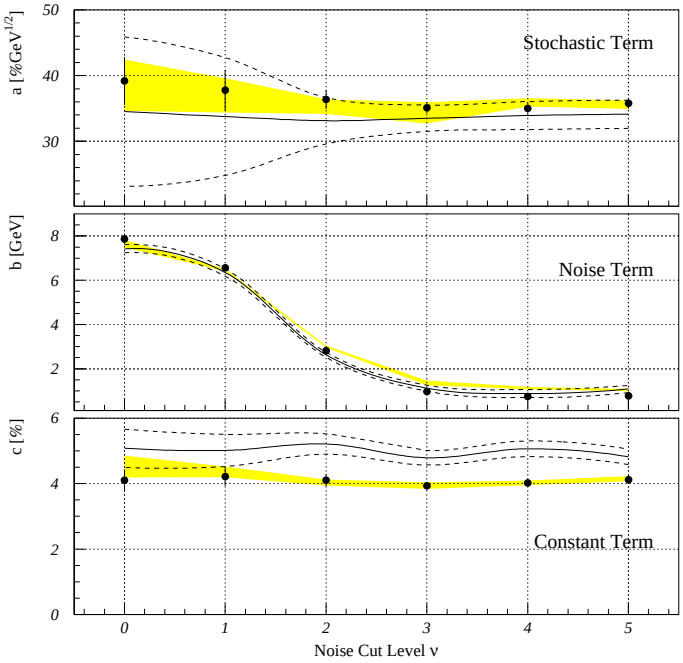

Figure 19: *Contributions to the relative energy resolution, as fitted using eq.(6), as function of the noise cut ν. The full circles are experimental data, the shaded area indicates the GEANT3 values and their errors, and the solid line represents the GEANT4 values, with the dotted lines showing the corresponding error.*

contribute their full signal, even if some of their area is outside. This makes the cluster signal dependent on where the impact point, which determines the cylinder location, is located with respect to the tile centers.

One way to avoid the corresponding (somewhat arbitrary) signal fluctuations is to allow fractional signal contributions $w \cdot E_{rec}^{tile}$ to the cluster, according to the following scheme:

$$w = \begin{cases} 1 \quad \ldots\ldots\ldots & \text{for tiles completely inside the cylinder;} \\ \sqrt{A_{shared}/A_{tile}} & \text{for tiles partly inside the cylinder;} \\ 0 \quad \ldots\ldots\ldots & \text{for tiles completely outside of the cylinder.} \end{cases} \tag{7}$$

A_{shared} is the area of the tile covered by the cylinder ($0 \leq A_{shared}/A_{tile} \leq 1$), while A_{tile} is the tile area. The definition of the signal weight w in the equation above is chosen such the energy resolution for the cluster is optimal. Figure 20 shows the integrated radial shower profile for electrons in FCal1 Module 0, and the relative energy resolution as function of the cluster radius. Collecting signal beyond a radius of about $6 - 8$ cm does obviously not add to the signal anymore, but increases the fluctuations due to noise pick-up. A careful analysis of the profile actually shows a decrease of the cluster signal with increasing radius, which indicates negative signal crosstalk around the electromagnetic shower[9]. Table 2 shows quantitative estimates for this crosstalk effect. Note that the experimental data is calibrated for the total signal, which corresponds to $E(r = \infty)$ in the table.

[9] the source of this crosstalk has not been completely isolated. The most likely candidate is the analog front

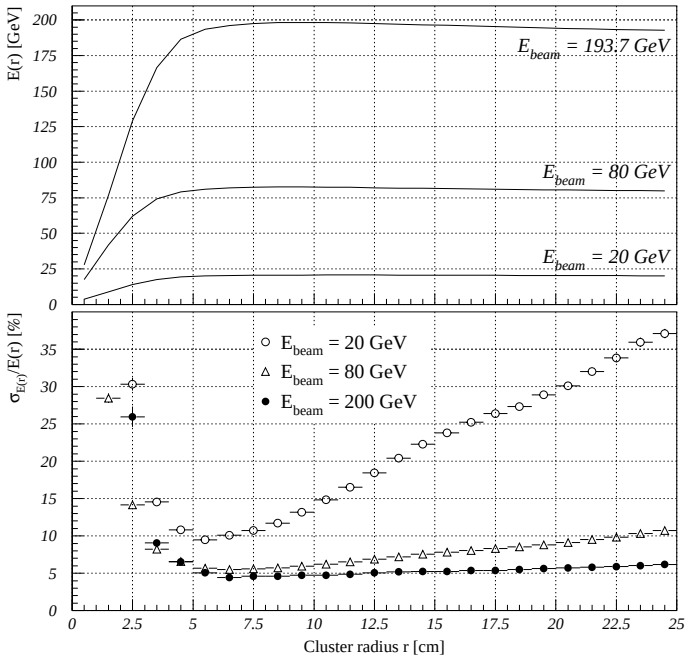

Figure 20: *Integrated radial shower profiles for experimental electrons of different beam energies in FCal1 Module 0 (upper plot). The lower plot shows the relative energy resolution $\sigma_{E(r)}/E(r)$ as function of the cluster radius r. The radial acceptance of the module changes around r = 15 cm, as part of the cluster cylinder area is outside of the instrumented calorimeter region for these larger radii. See text for further remarks on these plots.*

Fitting the resolution function in eq.(6) for each cluster radius yields the parameters shown in Figure 21. These fits only make sense for radii larger than about 4 cm, as the signal distribution for smaller clusters is very non-gaussian. A cluster size between 4 and 6 cm still does not sample a sufficient fraction of the shower energy for a linear response at optimal resolution. Cluster radii between $6-7$ cm seem to be ideal (see table 3 for resolution parameters). Larger clusters start to pick up noise, which clearly causes the energy resolution to deteriorate.

6.5 Optimal energy resolution

The inhomogeneous FCal1 front face suggests corrections of the signal depending on the impact point. This impact point is rather well known (typically within ±0.5 mm or better in each transverse dimension) from the reconstructed track for each particle. The electron signal has been studied as a function of the impact point coordinate, and correction factors have been calculated and stored in correction tables. These tables are then used to correct the signal for each event, depending on the actual impact position.

Figure 22 shows the effect of this impact point correction on the relative energy resolution for electrons in FCal1 Module 0. The constant term is improved by nearly a factor of two (see also table 3). This measurement is an attempt to determine the best possible

end board, see section 3.

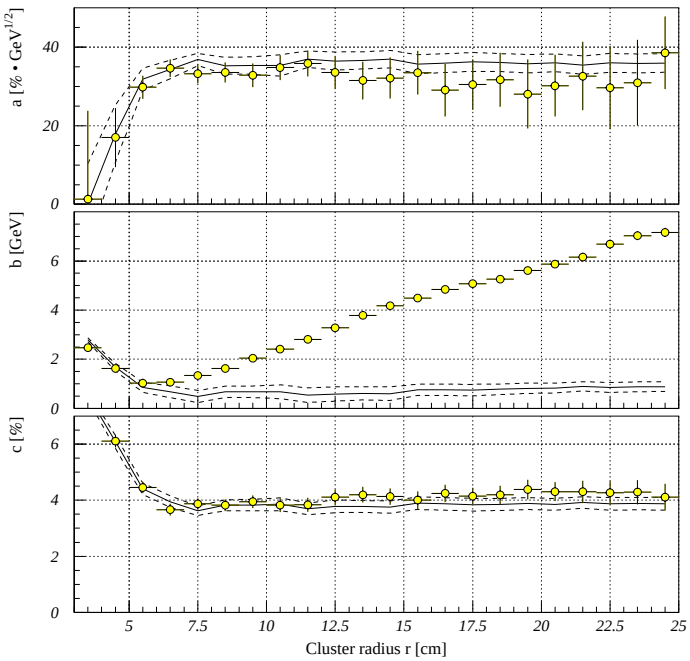

Figure 21: *Results from fits to the electron energy resolution function given in eq.(6), for different cluster sizes r (experimental data only). The upper plot shows the stochastic term a as function of r, while the plot in the middle shows the noise term b, which increases with larger cylinder radius, as expected. The constant term c is, very much like a, only slightly depending on the cluster size, at least for clusters large enough to sample a very large fraction of the electromagnetic shower. The solid lines indicate the fit results if a noise cut $\nu = 3$ is applied, while the dashed lines show the corresponding errors.*

Beam Energy [GeV]	$\Delta E/E(r=\infty)$ [%]	ΔE [GeV]
20.0	2.80±0.86	0.56±0.17
40.0	3.11±0.33	1.24±0.13
60.0	2.97±0.23	1.79±0.14
80.0	3.37±0.19	2.70±0.15
193.7	2.85±0.23	5.50±0.45

Table 2: *Crosstalk around the electromagnetic shower in FCal1 Module 0, estimated by the maximum cluster signal E_{max} and the signal for an infinitely large cluster $E(r=\infty)$, with $\Delta E = E_{max} - E(r=\infty)$.*

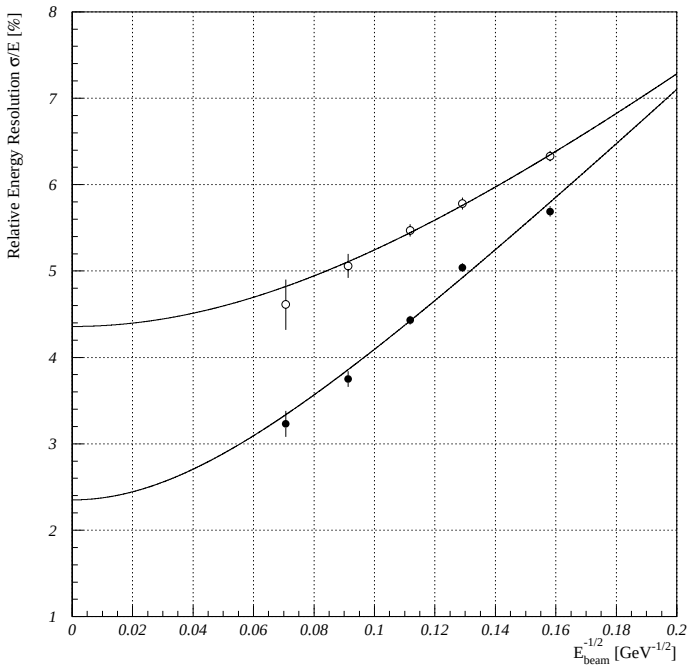

Figure 22: *The relative energy resolution for electrons in FCal1 Module 0, as measured in the test beam, as function of* $1/\sqrt{E_{beam}}$. *The open circles show uncorrected data, while the full circles show the resolution after impact point corrections. The noise is in both cases unfolded. The lines show results from fits of eq.(6) to the data (without the noise term b).*

intrinsic resolution of the FCal, and therefore represents the optimum in performance for this particular calorimeter.

6.6 Impact point reconstruction

ATLAS does not provide track measurements in front of the FCal, which means that in this case the impact point has to be determined from calorimeter signals themselves. A straight forward center of gravity method only allows a rather coarse measurement, as shown in Figure 23. The tile size is rather large compared to the lateral size of an electromagnetic shower, which tends to pull the reconstructed center of gravity toward the tile centers (Figure 23(a)).

	Resolution Fits		σ/E (193.7 GeV)
	a $[\% \cdot \sqrt{\text{GeV}}]$	c [%]	[%]
raw	29.19 ± 1.23	4.34 ± 0.15	4.61 ± 0.29
corrected	33.51 ± 0.71	2.35 ± 0.16	3.43 ± 0.15
cluster ($r = 7$ cm)†	34.60 ± 2.24	3.66 ± 0.21	4.43 ± 0.11

Table 3: *Energy resolution fit parameters for experimental electron data (see eq.(6)), with and without the impact point correction, and for a cylindrical cluster of 7 cm radius. The relative energy resolution for the highest available energy is given in addition.*

Careful analysis actually shows that even electrons with a very large fraction of the signal in just one tile seem to have their center of gravities slightly off from the corresponding tile center, which is due to the small incident angle of the particles.

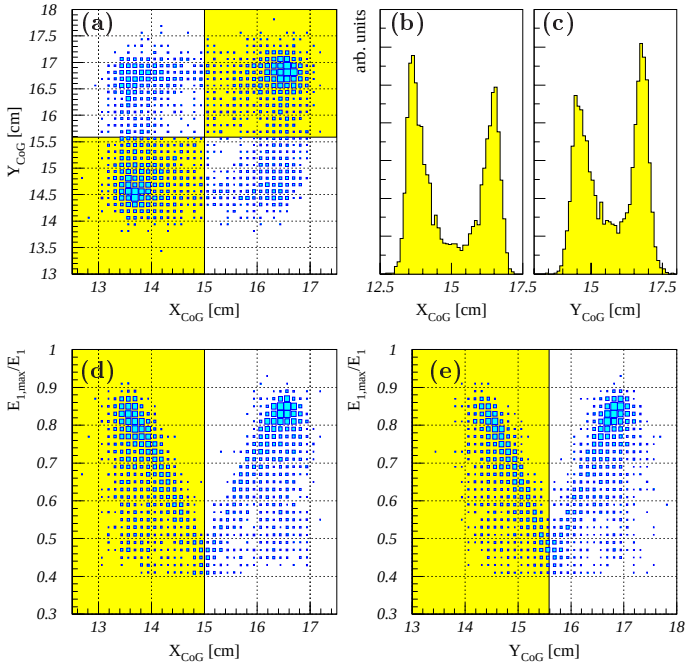

Figure 23: *The distribution of the center of gravities for 80 GeV electron showers on the front face of FCal1 Module 0 (a). The gray and white boxes indicate tiles (readout channels). The distributions of the horizontal (X_{CoG}) and vertical (Y_{CoG}) center of gravity coordinates are shown in (b) and (c), respectively. Figure (d) shows the ratio of the maximum signal in one tile $E_{1,max}$ over the total signal in FCal1 E_1, plotted as function of the horizontal coordinate. The same ratio as function of the vertical coordinate is shown in (e).*

A more evolved method for impact point reconstruction explores the spatial signal pattern generated by the lateral electromagnetic shower spread in the FCal1 readout tiles, and its relation to the impact point. This method consists of two steps. In a first step the signal sharing variable

$$F_{ij} = \frac{E^i - E^j}{E^i + E^j} \tag{8}$$

is calculated for each tile pair $(i, j, i \neq j)$ in electron events. Only pairs with significant tile signals E_i, E_j are considered. F_{ij} is then binned in steps of typically 0.2 for $-1 \leq F_{ij} \leq 1$, thus producing a characteristic feature of the pattern. The other feature used to classify the pattern is the geometrical relation between the two tiles in a given pair. These relations are common edge left/right or up/down[10], common corner points (top, left)/(top, right), (bottom, left)/(bottom,right), separated by one or two tile(s) (left, right, top, bottom, or along a diagonal), and others. The impact point coordinates from the tracking system are then stored for each F_{ij} bin, and each geometrical tile relation, producing patterns as shown in

[10]the tiles are actually rectangles, i.e. left/right is different from top/bottom.

Figure 24. Similar patterns of many events are overlaid to calculate the probability contours for the impact point. Finally, the combined probability for all geometrical relations and F_{ij} bins is calculated by adding the logarithms of the individual probabilities.

In the reconstruction step the pattern characteristics of a given event are calculated in the same space of F_{ij} bins and geometrical relationships. The most likely impact point is then looked up in the probability contours for the found pattern. It must be pointed out that the probability contours are calculated from 193.7 GeV/c electrons, and then applied to all other energies. No significant energy dependence of the patterns is expected, at least not at a level significant for the impact point reconstruction, as the lateral shower profiles show only a very slight energy dependence themselves. Finally, this method makes optimal use of the tile segmentation, and is certainly less sensitive to the relation between lateral tile and shower size than the center of gravity approach.

Using the impact point reconstructed this way for signal corrections does not improve the energy resolution significantly, but does allow an estimation of the space resolution for electrons in the FCal. Figure 25 shows the radial and azimuthal (tangential) space resolution as function of the beam energy. Fitting a resolution function

$$\sigma_s = \frac{a_s}{\sqrt{E_{beam}}} \oplus \frac{b_s}{E_{beam}} \oplus c_s, \tag{9}$$

where a_s is the stochastic, b_s the noise, and c_s the constant term, to the radial ($s = r$) and azimuthal ($s = t$) space resolution yields

$$a_r = (10.58 \pm 0.23)\ \text{mm} \cdot \sqrt{\text{GeV}}, \quad b_r = (42.0 \pm 1.4)\ \text{mm} \cdot \text{GeV}, \quad c_r = (1.10 \pm 0.02)\ \text{mm};$$
$$a_t = (8.02 \pm 0.16)\ \text{mm} \cdot \sqrt{\text{GeV}}, \quad b_t = (46.9 \pm 0.8)\ \text{mm} \cdot \text{GeV}, \quad c_t = (0.57 \pm 0.02)\ \text{mm}.$$

This corresponds to a high energy limit in the resolution of the pseudo-rapidity measurement $\sigma_\eta \approx 0.009$ at $|\eta| = 3.7$ for single electrons in the FCal[11]. The uncertainty in azimuth at the same pseudo-rapidity is $\sigma_\varphi \approx 2.4$ mrad. These estimates are certainly rather optimistic for the FCal in ATLAS, where the incoming energy is typically carried by jets, rather than single particles. This means less significant signals, especially in the presence of pile up, which should deteriorate the spatial resolution. On the other hand, the jet signal should be less sensitive to the impact point, as the energy is already somewhat distributed in space before even reaching the FCal. A first experimental hint of this effect has already been observed with the very first FCal prototype in 1993, where small amounts of additional inactive material, put into the electron beam to produce "target jets", lead to an improvement in the constant term of the energy resolution [6].

6.7 Signal composition

The energy sharing across tiles in electromagnetic showers can be a sensitive test for the signal composition in the experiment and simulation. The tile signal spectra, accumulated over a large number of electron events, can provide a global measure of the signal composition. To unfold differences in the sensitivity of individual tiles, which are mainly due to gain fluctuations in the electronics, the *cell signal significance* measurement Γ is used:

$$\Gamma = \frac{E_{rec}^{tile}}{ENE^{tile}}. \tag{10}$$

[11] longitudinal vertex smearing in ATLAS is not included in this estimate.

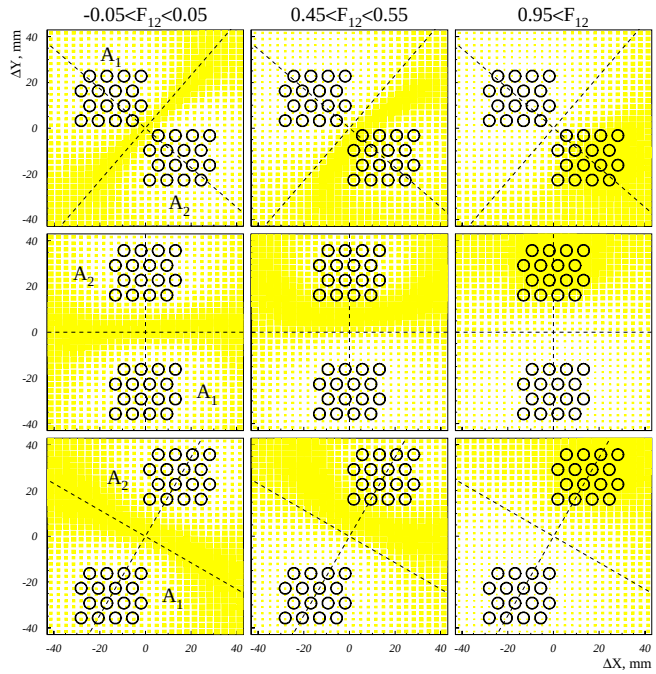

Figure 24: *Distributions of impact points on the FCal1 front face for three different bins of the signal sharing variable F_{ij} and three different geometrical relations between the paired tiles: "bottom right" in the top row, "top separated by one" in the middle row, and "top right separated by one" in the bottom row.*

Figure 26 shows the distribution of Γ for 60 GeV/c electrons. It is obvious that higher significance signals occur more often in the experiment than in either Monte Carlo, i.e. the electromagnetic showers are more dense. Accordingly, the composition of the total energy from tile energies is somewhat softer for the simulations, as can be seen in the lower plot of the same figure. The GEANT3 and GEANT4 simulation obviously compare very well with each other with respect to signal composition. The differences between the two simulations in the energies reconstructed for different noise cuts (see paragraph 6.2, Figure 15) probably have their origin in very subtle differences in the shapes of these spectra.

7 Conclusions and Outlook

Results from a detailed study of the electron response of the ATLAS Forward Calorimeter, using both experimental data from the 1998 Module 0 testbeam and simulations within the GEANT3 and GEANT4 frameworks, have been presented in this note. Important performance parameters like signal linearity for electron energies from 20 to 200 GeV, and energy resolution in the same energy range, are found to be well within the requirements for ATLAS physics: deviations from linearity are within $\pm 1\%$, and the most important high energy limit in the energy resolution is of order 4%.

Direct comparisons of the experimental data with the two different simulations indicate that the average signal as a function of the electron energy can be understood at the level of one percent. There are significant differences, though, in some details of the shower

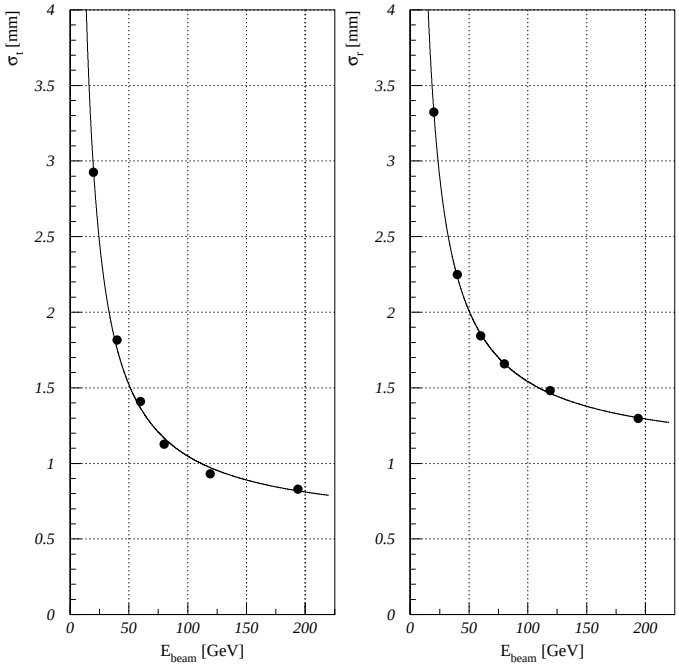

Figure 25: *The azimuthal (σ_t, left) and the radial (σ_r, right) space resolution for electrons in FCal1 Module 0, as function of the beam energy. The resolution of the tracking system used in the test beam is unfolded from the experimental data. The curves show results of fits of the resolution function given in eq.(9).*

development. The showers reconstructed from the experimental data seem to be narrower with higher signal densities, as can be seen in the comparisons of cell signal significances and lateral shower profiles. GEANT3 and GEANT4 on the other hand agree very well with each other.

These observations are partly supported by the signal dependence on cell filters like noise cuts. GEANT3 simulations lose significantly more "true" signal to this cut than measured in the experiment, between 2% for a 5σ noise cut at 200 GeV/c electron momentum, and 4% at 20 GeV/c with the same noise cut. On the other hand, GEANT4 simulated signals follow the experimental signals as function of the noise cut quite well.

The understanding of the simulation signal can probably be improved by some tuning of the dimensions in the geometry description, which is possible within the mechanical tolerances of the real module. This can help to adjust the volume sampling fraction. Other uncertainties are possible in the description of the material compositions, which affect basic calorimeter characteristics like the dE/dx weighted sampling fraction and the effects of material transitions on the signal. There is much less room for tuning here, though, especially in the most important electromagnetic FCal1 module, which consists of pure copper. Effects from an insufficient accuracy in the description of the testbeam environment, mainly due to lack of knowledge of the precise distribution of inactive material in front of the calorimeter, is unlikely to contribute significantly to the differences between data and simulations.

The results of the 1998 FCal Module 0 testbeam for electrons generally indicate a good performance of this calorimeter well within the physics requirements for ATLAS. It has

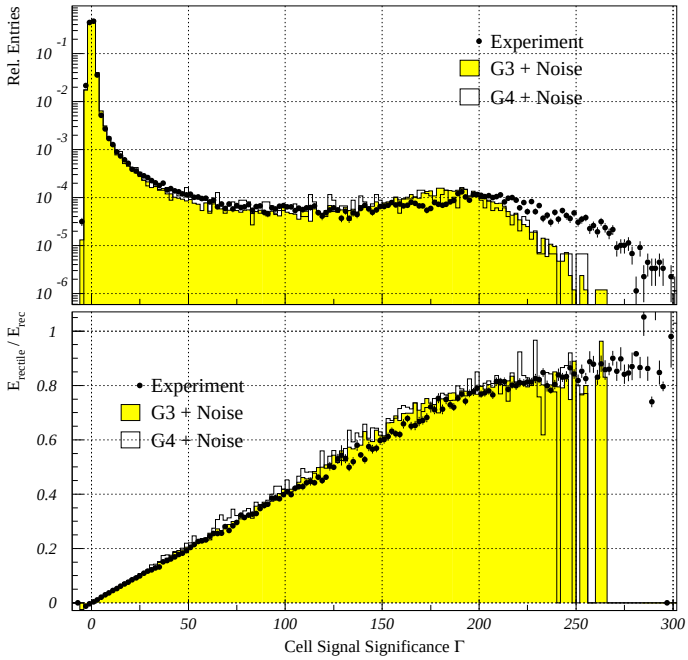

Figure 26: *The tile signal significance distribution for 60 GeV/c electrons in FCal1 Module 0 (upper plot). The peak on the left is centered around 0 and has a width of 1 on this signal scale. It contains tiles which do not contribute to the electron signal. The electron shower signals are in the tail of this distribution. The lower plot shows the relative contribution of tile signals with a given* Γ *to the total signal.*

also been shown that the GEANT4.0.2R2 Detector Simulation Toolkit is a mature software package, capable of describing the most relevant features of the FCal electron signal with at least the same quality as GEANT3.21. Remaining discrepancies between data and both simulations are under study.

Acknowledgments

We are very grateful to the ATLAS Liquid Argon and Testbeam communities for their help with the FCal Module 0 testbeam effort in 1998. In addition, we like to thank M. Donkers, D. Paterson, D. Waller (all Carleton University, Ottawa), J. Kamnitzer and W. Trischuk (both University of Toronto) for their contributions. We also like to thank members of the CERN staff for their support, especially N. Doble and K. Elsener for providing excellent beams for this experiment. P. Gumplinger, J. Apostolakis and other members of the GEANT4 collaboration and the ATLAS-GEANT4 Comparison Project provided a lot of help with GEANT4, which we thankfully acknowledge. Last but not least we like to thank our funding agencies for their continuing support.

References

[1] ATLAS Liquid Argon Coll., *Liquid Argon Calorimeter Technical Design Report*, CERN/LHCC/96-41 (1996); ATLAS Coll., *ATLAS Calorimeter Technical Design Report*, CERN/LHCC/96-40 (1996); ATLAS Coll., *ATLAS Detector and Physics Technical Design Report*, CERN/LHCC/99-14/15 (1999).

[2] A. Savine *et al.*, in *Proc. Vth Int. Conf. on Calorimetry in High Energy Physics, Upton, New York 1994*, ed. H.A. Gordon and D. Rueger (World Scientific, Singapore 1995).

[3] J.P. Rutherfoord, in *Proc. VIth Int. Conf. on Calorimetry in High Energy Physics, Frascati 1996*, ed. A. Atonelli, S. Bianco, A. Calcatera and F.L. Fabbri (Frascati Physics Series, Vol. 6, 1996).

[4] J. Armitage *et al.*, in *Proc. 5th Int. Conf. on Advanced Technology and Particle Physics, Como 1996*, ed. E. Borchi, S. Majewski, J. Huston, A. Penzo, and P.G. Rancoita, Nucl. Phys. B (Proc. Suppl.) 61B 101-105 (1998).

[5] J. Dubeau *et al.*, in *Proc. 5th Int. Conf. on Advanced Technology and Particle Physics, Como 1996*, ed. E. Borchi, S. Majewski, J. Huston, A. Penzo, and P.G. Rancoita, Nucl. Phys. B (Proc. Suppl.) 61B 95-100 (1998).

[6] M.I. Ferguson *et al.*, *Nucl. Instrum. Methods* A **383**, 399-408 (1996).

[7] J.K. Mayer *et al.*, in *Proc. VIIth Int. Conf. on Calorimetry in High Energy Physics, Tucson, 1997*, ed. E. Cheu, T. Embry, J. Rutherfoord, and R. Wigmans (World Scientific, Singapore, 1998).

[8] P. Loch and P. Savard, in *Proc. VIIth Int. Conf. on Calorimetry in High Energy Physics, Tucson, 1997*, ed. E. Cheu, T. Embry, J. Rutherfoord, and R. Wigmans (World Scientific, Singapore, 1998).

[9] A. Savine *et al.*, in *Proc. VIIth Int. Conf. on Calorimetry in High Energy Physics, Tucson, 1997*, ed. E. Cheu, T. Embry, J. Rutherfoord, and R. Wigmans (World Scientific, Singapore, 1998).

[10] P. Savard, Thesis, University of Montreal (1997).

[11] P. Loch, in *Proc. VIIIth Int. Conf. on Calorimetry in High Energy Physics, Lisbon, 1999*, ed. G. Barreira, A. Gomes, A. Maio, B. Tome, and M.J. Varanda (World Scientific, Singapore 2000).

[12] R. Brun and F. Carminati, *GEANT Detector Description and Simulation Tool*, CERN Programming Library Long Writeup W5013 (1993).

[13] GEANT4 Coll, `http://wwwinfo.cern.ch/asd/geant4/geant4.html`

[14] P. Loch, *Tube Radius Optimization for the ATLAS Electromagnetic Forward Calorimeter*, ATLAS Internal Note LARG-NO-39 (1996).

[15] R.L. Chase, C. de la Taille, S. Rescia and N. Seguin-Moreau, *Nucl. Instrum. Methods* A **330**, 228-242 (()1993); R.L. Chase, C. de la Taille and N. Seguin-Moreau, *Nucl. Instrum. Methods* A **343**, 598-605 (1994); C. de la Taille, in *Proc. Int. Conf. on Advanced Technology and Particle Physics, Como 1992*, Nucl. Phys. B32 449-459 (1993).

[16] P. Loch, *Suggestions for a General Energy Reconstruction Scheme for the ATLAS Calorimeters*, ATLAS Internal Note CAL-NO-91 (1997); H1 Calorimeter Group (B. Andrieu et al.), *Nucl. Instrum. Methods* A **350**, 57-72 (1994).